https://doi.org/10.1016/j.carbon.2019.10.045

Advanced lignin-derived hard carbon for Na-ion batteries and a comparison with Li and K ion storage

Xiuyi Lin[†, a], Yizhe Liu[†, a], Hong Tan[a,b], Biao Zhang[a,b*]

[a]*Department of Applied Physics, The Hong Kong Polytechnic University, Hung Hom, Hong Kong, P.R. China.*

[b]*The Hong Kong Polytechnic University Shenzhen Research Institute, Shenzhen, P.R. China*

[†]: These authors contributed equally to this work

Abstract

Hard carbon is the most attractive anode in Na-ion batteries. The performance of hard carbon relies primarily on the precursors and the synthesis approaches. Lignin, as the second-abundant biopolymer in nature, with the low cost and high carbon yield make it an ideal precursor for the preparation of hard carbon. However, lignin-derived hard carbon from direct carbonization shows poor electrochemical performance. A low-temperature pre-oxidation is applied in this study to introduce carbonyl groups for enhancing the crosslink of lignin. Consequently, the growth and orientation of graphitic layers during carbonization are inhibited, which in turn increases the layer distance for facilitating the Na ion insertion and leads to exceptional rate capability and superb cyclic life. To gain insights into the charge storage mechanism, a comparison with Li- and K-ion storage in hard carbon is conducted through in-situ Raman tests. There are similarities of alkali-metal ion storage at high voltages but remarkable disparities at low voltages, thus emphasizing the importance of microstructure design of hard carbon depending on the application in various metal-ion batteries.

Keywords: hard carbon, anodes, in-situ characterization, Na-ion batteries

[*]Corresponding author: Tel: (+852) 34003260. Email address*:* biao.ap.zhang@polyu.edu.hk (Biao Zhang)

1. Introduction

The ever-growing energy storage market has raised concerns on the sustainability of Li-ion batteries (LIBs) and caused a price surge on the lithium sources. Na-ion batteries (NIBs) are therefore revived thanks to the natural abundance of sodium element and its geographically even distribution. Together with the capability of using Al foil as a current collector on the anode side, NIBs are expected to possess advantages in the cost, making them promising candidates in stationary energy storage.[1–3] The primary issue afflicting NIBs is the low energy density of around 120 Wh kg^{-1} (in the prototype cell level) at this stage, in comparison with over 200 Wh kg^{-1} for LIBs.[4] Intensive studies are therefore focused on developing novel electrode materials that could offer higher energy. Several promising cathodes have been designed such as Prussian-blue analogous $Na_2M_aM_b(CN)_6$,[5–7] polyanionic $Na_3V_2(PO_4)_2F_3$ compounds,[8,9] and P2-type or O3-type layered oxides (e.g., $Na_{0.7}Fe_{0.5}Mn_{0.5}0_2$).[10–12] The composition, structure, and charge/discharge protocol of these compounds are optimized to gain more capacities and to improve the cyclic stability.[8] Hence synchronous study is necessary for the anodes, where hard carbon and alloys are among the most attractive candidates.

Hard carbon represents a type of carbon materials that are difficult to be graphitized due to the presence of various sp3 structure in the precursors, which inhibits the orientation and growth of graphene layers during the carbonization and graphitization processes. Consequently, hard carbon consists of randomly located curved graphitic layers with a considerable amount of nanopores presented, rendering plenty of active sites for Na ion storage to achieve a capacity of ~300 mAh g^{-1}.[13,14] Biomass and polymers are the two most popular types of precursors in synthesizing hard carbon. Being natural abundant and environmentally friendly, biomass wastes such as rice husk, lychee, date palm and longan peels have been widely adopted, and the resulted hard carbon delivers competitive performance.[15–18] Despite these advantages of biomass waste, the inconsistent quality of the precursors would result in the disparities in the capacities between batches and thus bring about difficulties in large-scale production. Researchers are questioning which component in the biomass plays a vital role. A systematic study by Passerini et al. shows the lignin-rich precursor presents higher capacity than hemicellulose- and pectin- rich counterpart does.[19] Lignin also has a carbon yield of over 50 wt.%, making it an ideal precursor for hard carbon preparation.[20] Nevertheless, neat lignin-derived hard carbon fails to deliver a decent performance, and hybridization with other precursors like pitch and polyacrylonitrile is needed to

improve the capacities.[21,22] Recent work indicates the grade of lignin is important in determining the as-prepared hard carbon. A capacity of approximately 280 mAh g^{-1} is obtained through optimized synthesis approaches, but the cyclic stability requires further improvement.[23] In this study, we employ a simple pre-oxidation to modify the structure of lignin precursor, which significantly enhances the performance of as-prepared hard carbon. Furthermore, the detailed Na ion storage mechanism in hard carbon is still under debate. A comparison between Li, Na, and K ion storage behavior is also carried out, which is expected to offer some insights into the fundamental understanding of charge storage mechanisms.

2. Experimental

2.1 Materials synthesis

Commercially available alkali Lignin (Kraft, Sigma-Aldrich Cor.) was used as a precursor for producing hard carbon. Before carbonization, the precursor was pre-treated by oxidation in the air to modify the cross-linking structure. Typically, five grams brown powder of reagent-grade lignin was annealed in air at different temperatures of 150 °C, 200 °C, and 250 °C for 24 h at a heating rate of 5 °C min^{-1} with a muffle furnace. The obtained materials were denoted as LK-150, LK-200, and LK-250, respectively, which were further carbonized at 1350 °C for 2h under Ar stream at a heating rate of 2 °C min^{-1} with a tube furnace. After naturally cooling down to the room temperature, the obtained samples were denoted as LK-150-1350, LK-200-1350, and LK-250-1350, respectively. Lignin kraft without pre-oxidation was also carbonized at the same condition, which was denoted as LK-1350.

2.2 Materials characterization

The structure of hard carbon was characterized by X-ray diffraction (XRD) using a Rigaku SmartLab with a Cu Kα radiation source. Raman spectra were obtained using a Witec-Confocal Raman system (UHTS 600 SMFC VIS) with a laser wavelength of 532nm. The morphologies of the lignin and obtained samples were examined by TEM (JEOL 2010F) and SEM (JEOL-6490). The surface area and porous structure were analyzed by nitrogen adsorption-desorption measurements (ASAP 2020). Fourier transform infrared spectroscopy (FTIR) analysis was conducted on a Thermo Nicolet 380 FT-IR. Powder samples were mixed with KBr to form a translucent pellet for sampling. The composition of C, H, O and S was determined with a Vario EL III Element Analyzer (elementar Analysensysteme GmbH). Thermogravimetric analysis

(TGA) was conducted using TGA/DSC3+ (Mettler Toledo) from 80 to 600 °C with a heating rate of 10 °C min^{-1} in air.

2.3 Electrochemical measurement

All the electrochemical performances were tested in coin cells (CR2032) by using a hard carbon electrode as the working electrode and a Na metal sheet as the counter electrode. The as-prepared hard carbon powder was mixed with conductive carbon black and sodium alginate binder at a weight ratio of 90:5:5 in the deionized water to form a slurry, and then the resulting slurry was coated onto a copper (Cu) foil and dried at 80 °C overnight under vacuum. Two types of electrolytes are adopted, i.e., 1.0 M $NaClO_4$ in propylene carbonate (PC) and 1.0 M $NaPF_6$ in diglyme. A piece of Whatman glass fiber was used as the separator. The cells were cycled on a Land BT2000 battery test system within the voltage range of 0-3V at a constant temperature of 25 °C.

3. Results and Discussion

3.1 Effect of pre-oxidation

The preparation process of hard carbon from lignin kraft and the digital photos of corresponding products are shown in Fig. 1a. The products obtained from different process presented considerably different macroscopic shape and structure. Under direct carbonization at 1350 °C without pre-treatment, the obtained product presented rigid block forms that were stiff to grind it into powder. In contrast, the hard carbon derived from precursors with pre-oxidation was more crumble and softer, indicating a remarkable effect of oxidation in the air on modifying the structure of lignin kraft. Systematical studies on the effect of pre-oxidation were conducted, with the gradually increased oxidation temperature, i.e., 150, 200, and 250 °C under atmosphere environment.

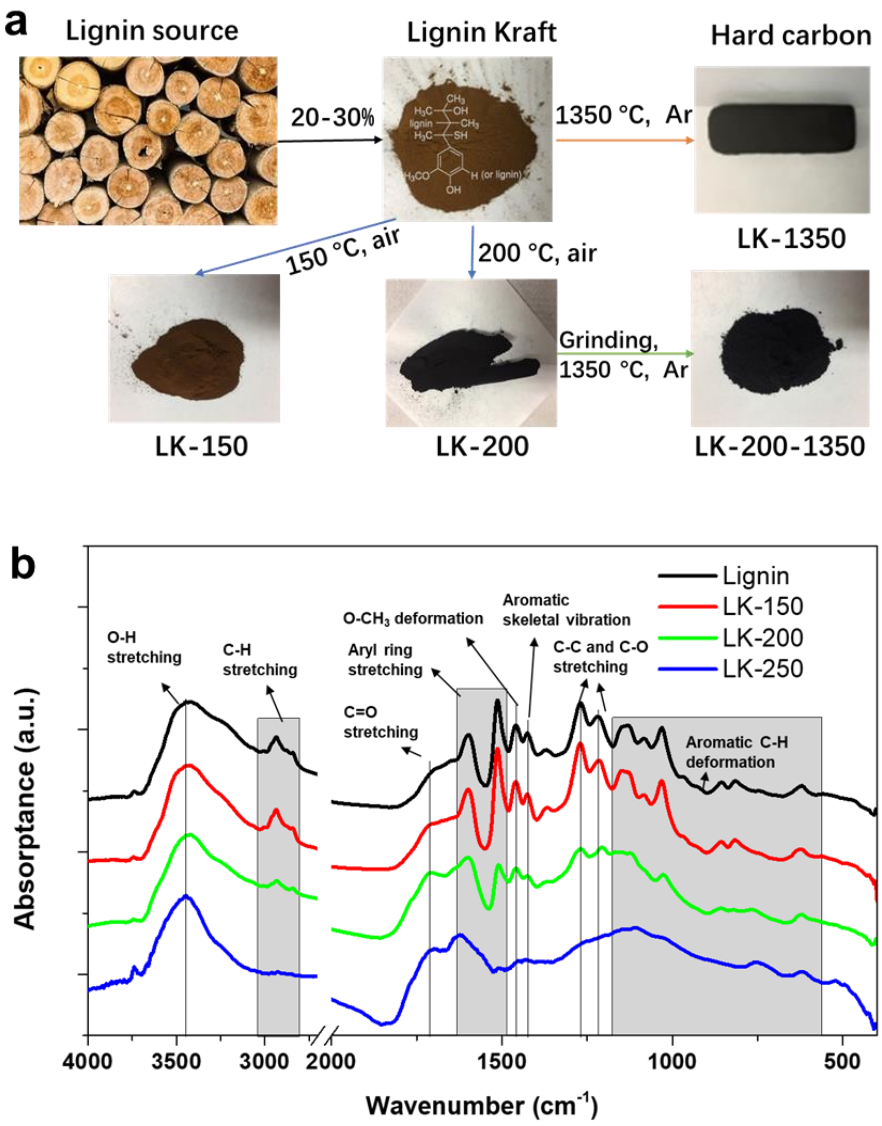

Fig. 1. (a) Preparation process of hard carbon derived from lignin kraft. (b) FTIR spectra of lignin kraft pre-oxidized at different temperatures.

FTIR spectroscopy measurements were employed to monitor the change of functional groups during the pre-treatment (Fig. 1b). In accord with the structure of lignin, the broad peak at 3450 cm^{-1} is assigned to O-H stretching. Other strong bands observed in pristine lignin are weakened after pre-treatment, including C-H stretching at 2933 cm^{-1} (in CH_2) and 2831 cm^{-1} (in CH_3); symmetric aryl ring stretching at 1956 cm^{-1}, asymmetric aryl ring stretching at 1510 cm^{-1}; aromatic C-H deformation at 980-1140 cm^{-1} (in-plane) and 610-860 cm^{-1} (out of plane). Regarding the lignin treated at 250 °C, these peaks become quite inapparent, indicating the removal of functional groups from an aromatic ring. On the contrary, a band represented C=O stretching at 1710 cm^{-1}

intends to increase with the pre-treatment temperature. These findings suggest the oxidation of alkyl groups and the formation of carbonyl groups during the pre-treatment. [24] The composition change after oxidation at various temperatures was further examined by elemental analysis. After treatment at 150 °C, both the oxygen and hydrogen content slightly decrease because of de-hydration (Table 1). The color of LK-150 remains brown, in comparison with the black color for LK-200 and LK-250 (Fig. 1a). This is consistent with the structural changes observed in FITR spectra, where LK-150 shows negligible alteration. A considerable amount of oxygen has been introduced into the structure after oxidation at 200 and 250 °C due to the formation of the C=O group, while the hydrogen content continuously decreases arising from the oxidation of alkyl groups. A severe drop of carbon content is found when treated at 250 °C, which attributes to the damage of the aromatic structure. TGA test shows that the lignin starts to decompose at above 200 °C and a significant mass loss between 300-400°C is observed (Fig. S1). Around 2% of sulfur exists in the precursor, which is speculated to be removed in terms of H_2S. Hence the amount of sulfur slowly decreases with increasing oxidation temperature.

Table 1 Elemental analysis of pristine lignin and oxidized lignin samples.

	C (%)	**H (%)**	**O (%)**	**S (%)**	**H/C**	**O/C**
Lignin	60.85	5.877	31.27	1.942	0.0966	0.5139
LK-150	61.97	5.492	29.87	1.739	0.0886	0.4820
LK-200	60.12	4.188	33.21	1.64	0.0697	0.5524
LK-250	54.41	3.013	39.05	1.569	0.0554	0.7177

After carbonization at 1350 °C, the morphology of the hard carbon was examined to figure out the influence of pre-oxidation. Typically, all the products are observed to have a granular microstructure with around 20-100 μm in size from SEM images (as shown in Fig. 2a-b, Fig. S2). LK-1350 has a dense and compact structure, while the morphologies are more porous and looser for the samples with pre-oxidation. Fig. 2 c-d display HRTEM images of corresponding hard carbon obtained by carbonizing lignin kraft and LK-200 at 1350 °C, respectively. Both reveal an assembly of curved layers, which are randomly intertwined together. There is no prominent long-range ordered structure in both LK-1350 and LK-200-1350. However, LK-200-1350 presents

some closed nanovoids surrounded by the curved graphene layers. Due to crosslinks in oxidized lignin, the graphitic domains tend to bend under high temperature instead of growing straight. These nanovoids may contribute to the large amount of micropores measured in the BET results and may introduce additional sodium storage sites through pore filling. In addition, the d-spacing of graphitic domains in LK-1350 is smaller than that in LK-200-1350 (Fig. 2c-d), suggesting the pre-oxidation process may prevent the growth of graphitic layers and allow larger interlayer space in hard carbon. [24,25] Nitrogen adsorption-desorption measurement was conducted to evaluate the effect of morphology differences on the surface area and pore size. LK-1350 and LK-200-1350 were measured since they have distinct shapes in SEM. The results suggest that LK-1350 has a Type II isotherm and a tiny surface area of 3.8 $m^2 g^{-1}$ (Fig. 2e), in agreement with the densely packed particles. The value increases to 30.9 $m^2 g^{-1}$ for LK-200-1350, while an unclosed hysteresis loop is observed showing a Type H4 isotherm according to the International Union of Pure and Applied Chemistry (IUPAC) classification. It seems that some nitrogen molecules are trapped in the narrow slit-like pores, causing the hysteresis. As a loose and porous structure of LK-200-1350 is observed in SEM (Fig. 2b), the pore collapse may occur during the experiment, which explains the open end at low pressure. The Density Functional Theory (DFT) model is used for pore size distribution. There are mainly in micropore (1-2 nm) and minorly mesopore (20-50 nm) in LK-200-1350, the large amount of micropores benefit the pore-filling of Na ion. Based on the above observations and the image processing of TEM results (Fig. S5), schematic illustrations presenting molecular structure of the hard carbons with and without pre-oxidation are given in Fig. 3a .

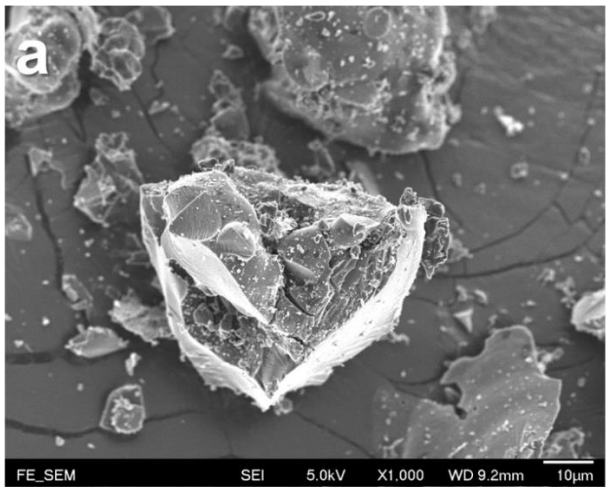

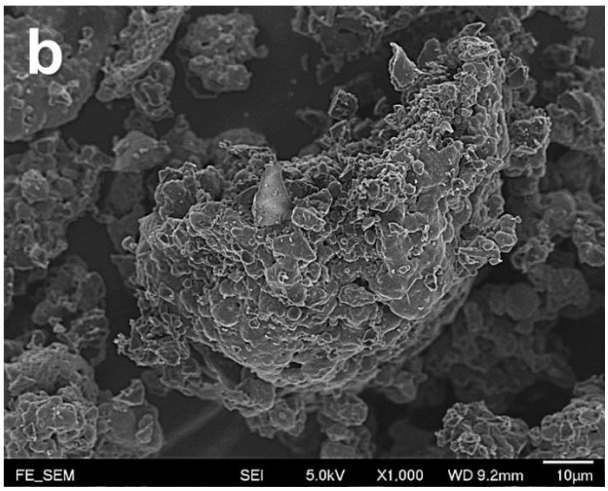

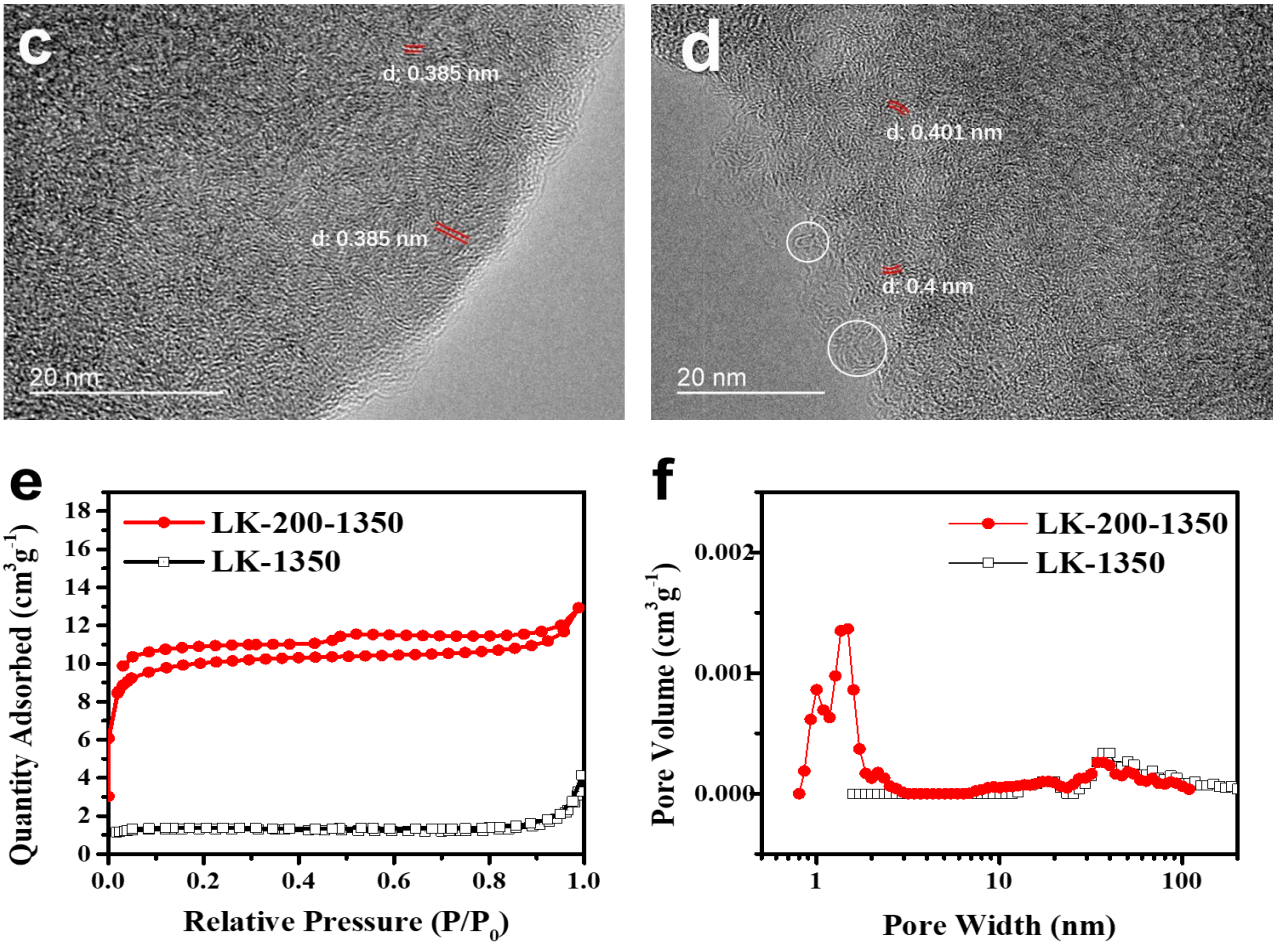

Fig. 2 SEM and TEM images of (a)(c) LK-1350 and (b)(d) LK-200-1350. (e) Nitrogen adsorption-desorption isotherms and (f) corresponding pore size distribution of LK-1350 and LK-200-1350.

To further investigate the effect of pre-oxidation, XRD patterns of the as-obtained samples are shown in Fig.3b. The two broad peaks around 23.0° and 44° can be assigned to the reflections of the (002) and (100) planes, showing the typically disordered carbon structure. The (002) peak located at a position of 2θ equal to 23.0°, corresponding to a d-spacing of 3.86 Å. The peak downshifts to 22.78° with pre-heating at 150 °C and further moves to the lower diffraction angle with increasing pre-oxidation temperature to 200 °C. The corresponding interlayer distance increases to 4.01 Å for LK-200-1350, in agreement with the TEM results. The dilated d-spacing would be beneficial to the insertion and extraction of Na ion in NIBs.

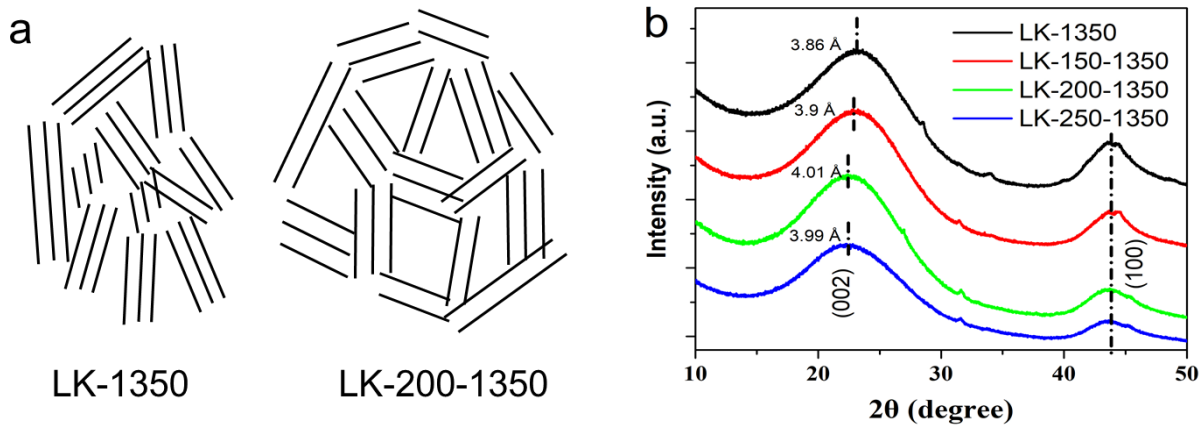

Fig. 3 (a) Schematic illustration of the molecular structure of hard carbons. (b) XRD of LK-1350, LK-150-1350, LK-200-1350, and LK-250-1350.

3.2 Electrochemical performance

The modification on the microstructure of hard carbon by pre-oxidation is expected to have a great impact on the Na ion storage. The electrochemical performances of the samples were accordingly evaluated in coin cells. We first tested the behaviors in the traditional carbonate-based electrolyte. The charge/discharge curves of the initial ten cycles at a current density of 25 mA g^{-1} in 1.0 M $NaClO_4$/PC electrolyte are plotted in Fig. 3a-b, and Fig. S3. A first discharge capacity of 324.5 mAh g^{-1} is obtained for the carbon directly carbonized at 1350 °C, followed by a charge capacity of only 232 mAh g^{-1}, which gives an initial Coulombic efficiency of 71.5%. With pre-oxidation, the Coulombic efficiency is significantly increased to 76.3% and 81.4% for LK-150-1350 and LK-200-1350, respectively. The initial irreversible capacity is usually associated with the formation of solid electrolyte interphase (SEI).[26] Although LK-200-1350 has a much higher BET surface area than LK-1350, the latter shows lower initial Coulombic efficiency. A previous study suggests that irreversible capacity in the first cycle could be divided into two parts, including SEI induced and non-SEI related.[27] The comparison between LK-1350 and LK-200-1350 indicates that a large part of the non-SEI related irreversible capacity is involved in LK-1350, caused by the trapping of Na ions in the dense and compact structure. The first charge capacity of LK-200-1350 is also increased by 32%, and a value of 307 mAh g^{-1} is achieved, among which around 200 mAh g^{-1} is contributed by the plateau at 0.1 V. However, an overheated oxidation temperature at 250 °C would deteriorate the performance, possibly due to the decomposition of

precursor (Table 1). Apart from that, it is delighted to find that all the samples possess excellent reversibility and negligible capacity fading is observed.

The electrochemical performance is then studied under various current densities. A fast capacity decrease is found at increasing rates, even for the sample LK-200-1350 (Fig. S4). It is ascribed possibly to the severe polarization in the presence of highly resistive SEI layer formed in the carbonate electrolyte. Since more than 60% of capacities are located at the low voltage plateau, the early termination due to polarization would exclude the capacity contribution at the region. To testify the assumption and fully exhibit the Na ion storage capability, an ether-based electrolyte, 1M $NaPF_6$ in diglyme, is adopted. The SEI formed in ether has proven thinner and more ionic conductive than that formed in carbonate,[28] thus rendering better rate performance for hard carbon anode. The capacity slightly increases to 336.4 mAh g^{-1} when charged at 25 mA g^{-1}. At higher current densities, glyme electrolyte shows great advantages, a capacity of 331.2, 322.3, 306.7, 291.3, 270.1 and 235.6 mAh g^{-1} is observed when cycled at 50, 100, 250, 500, 1000 and 2000 mA g^{-1}, respectively. The value obtained here is among the best for the reported hard carbon anode in Na-ion batteries, particularly under high current density, as shown in Table S1, The LK-1350 also possesses a reasonable performance in glyme, but the capacities at high currents substantially decrease. The capacity of LK-1350 remains only 62.6 and 29.2 mAh g^{-1} under the high current density of 1000 and 2000 mA g^{-1}, respectively. In addition to the electrolyte, the active material itself also play a critical role in the rate capability. The dilated layer distance and porous structure after pre-oxidation at 200 °C greatly facilitate the fast charge transfer, resulting in the exceptional capacity at high current densities. To test the long-cyclic stability, the LK-200-1350 electrode was charged/discharged at 200 mA g^{-1}. After 250 cycles, a capacity of 288.7 mAh g^{-1} is obtained. It is accounted for the 94 % of its first charge capacity at 200 mA g^{-1} (307.1 mAh g^{-1}), demonstrating superior stability towards long-cycle-life NIBs.

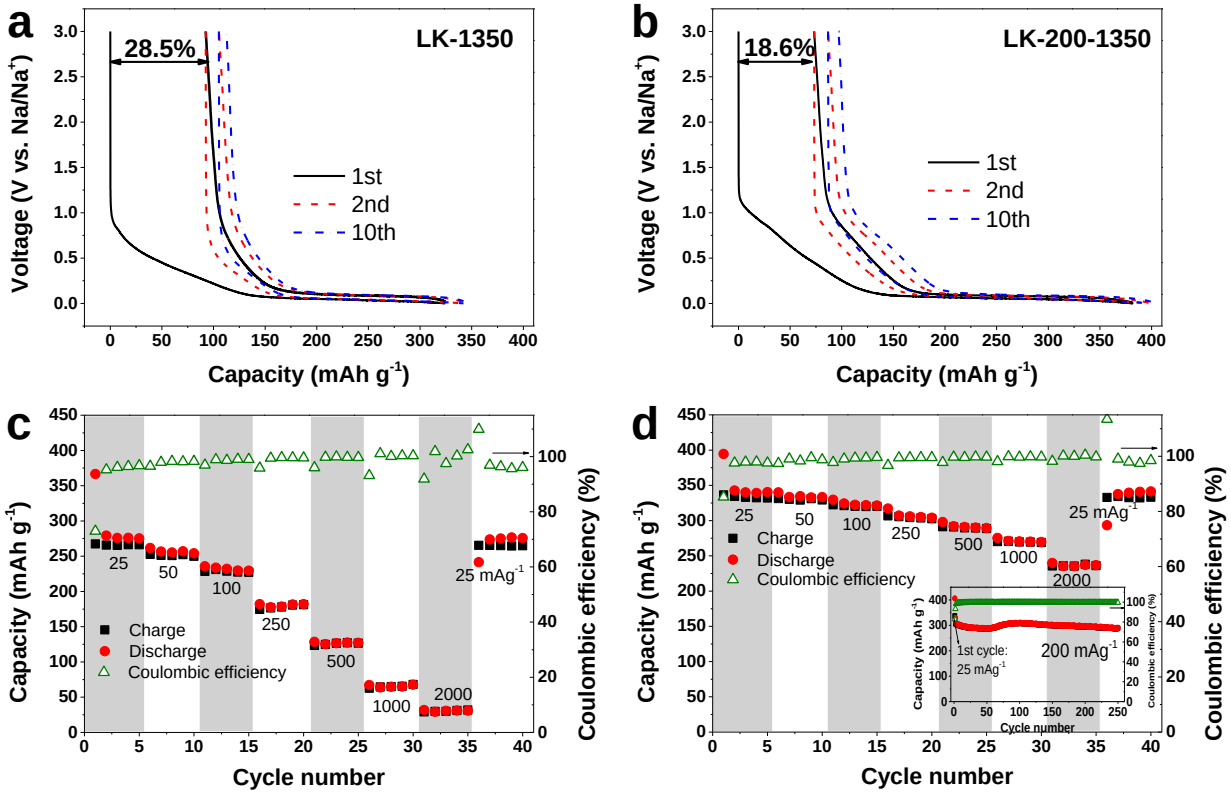

Fig. 4 Galvanostatic charge/discharge curves of (a) LK-1350 and (b) LK-200-1350. (Electrolyte: 1.0 M $NaClO_4$ in PC.) Rate capabilities of (c) LK-1350 and (d) LK-200-1350, inset is the cycling performance. (Electrolyte:1.0 M $NaPF_6$ in diglyme)

3.3 Charge storage mechanism

The Na ion storage mechanism in hard carbon has not reached an agreement yet. There is still a debate regarding the active sites associated with the low voltage plateau. Nanopore filling is proposed through a series of experimental, like in-situ XRD, ex-situ TEM and XPS. [29,30] Meanwhile, intercalation is observed by in-situ XRD, electron paramagnetic resonance, and ex-situ nuclear magnetic resonance.[31,32] A study also reported the intercalation of Na ion between graphene sheets in the low voltage plateau region first and then Na ion adsorption on pore surfaces. [33] Due to the poor crystallinity of hard carbon, it is difficult to detect the structural change from the position shift of diffraction peaks in XRD. An in-situ Raman test was thus conducted to examine the Na ion storage sites in the optimal sample, LK-200-1350. The Raman spectra of the sample charged/discharged to different states were collected as presented in Fig. 5. As widely

reported, the intercalation behavior would result in the apparent shape change of G band or even peak shift in the case of formation of low stage graphite intercalation compounds.[34–36] However, there is not any noticeable modification of D- and G- band of the sample during the whole cycle, ruling out the intercalation of Na ions in lignin-derived hard carbon. It shows identical mechanism as reported in hard carbon prepared from polyacrylonitrile, in which nanopores filling occurs in the 0.1 V plateau regime while the adsorption/desorption of Na ions leads to the sloping region between 0.1-1.5 V.[29,37]

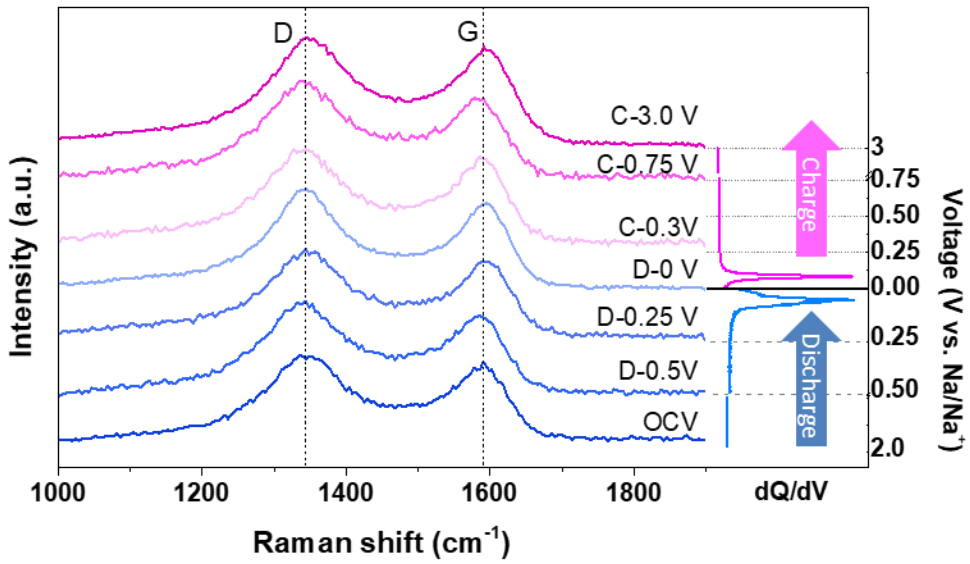

Fig. 5 Selective in-situ Raman spectra of LK-200-1350 with corresponding dQ/dV plot.

Besides Na ions, hard carbon is also able to store Li and K ions. Since alkali-metal ion storage behavior is similar in many respects, it would be interesting to compare their electrochemical performance and charge storage mechanism with different ion radii. The tests in Li-ion and K-ion batteries are also conducted in coin cells with the corresponding metal foil as a counter electrode. The voltage profiles of Li-ion storage are shown in Fig. 6a. In sharp contrast with those in NIBs, there is absent of any clear plateau. dQ/dV curves indicate the presence of two peaks located at 0.91 and 0.005 V (Fig. 6b). In-situ Raman spectra were collected in Fig. 6e to explore the Li-ion storage sites. Both the peaks of D- and G- band barely change until discharge to 0.25 V, due to the Li-ion adsorption on the isolated graphene layers [38]. With further discharge, the changes of Raman band may be divided into three stages: blue shift of the G band from 1590 cm^{-1} to 1600 cm^{-1} implying the beginning of li ion intercalation; the loss of D band attributed to the reordering of the graphite structure; and the significantly broadening of G peak to an asymmetric

fanoresonance shape due to interference between the metallic like behavior of low stage GICs. Nevertheless, lacking long-ranged graphene sheets leaded to partially intercalation in hard carbon, thus the capacity of Li-ion batteries is lower than that of NIBs. For the case in K-ion batteries, the low voltage plateau that shown in Na-ion batteries is also missing in the discharge curve. The voltage continuously decreases with more K ions uptake. The charge curve consists of two main sloping regions located at around 0.38 V and 0.11 V, as seen in the dQ/dV plot. The phenomenon is similar to our previous observation,[39] where K ion adsorption/desorption is the main mechanism as proven by density functional theory calculations. Indeed, the in-situ Raman spectra of hard carbon in K-ion batteries do not show obvious change during the full charge/discharge cycle, confirming the negligible contribution from intercalation. Pore filling of alkali metal ions is characteristic of low voltage plateau at a potential close to 0 V, the absence of the plateaus indicates the minimal capacity gain for K ion filling in the nanopores.

It can be concluded from the above comparison, that the ion adsorption/desorption on the randomly oriented graphene layers occurs for all the Li, Na and K ions, which is responsible for the capacity at high voltages (e.g., above 0.25 V vs. the corresponding metal electrode). However, different mechanisms govern the charge storage at the low voltage depending on the type of ions. The Na ion storage delivers the highest capacities, demonstrating the advantages of pore filling in the uptake of more ions. It seems that the requirement of pores for the pore filling mechanism varies with the nature of chargers. The reason for incapability of Li and K ions in the as-prepared hard carbon is not yet understood. Studies are ongoing in our group to explore the correlation between the properties of pores and the ability of uptake ions of different sizes, which may benefit the development of higher-capacity hard carbon anode for alkali metal-ion batteries.

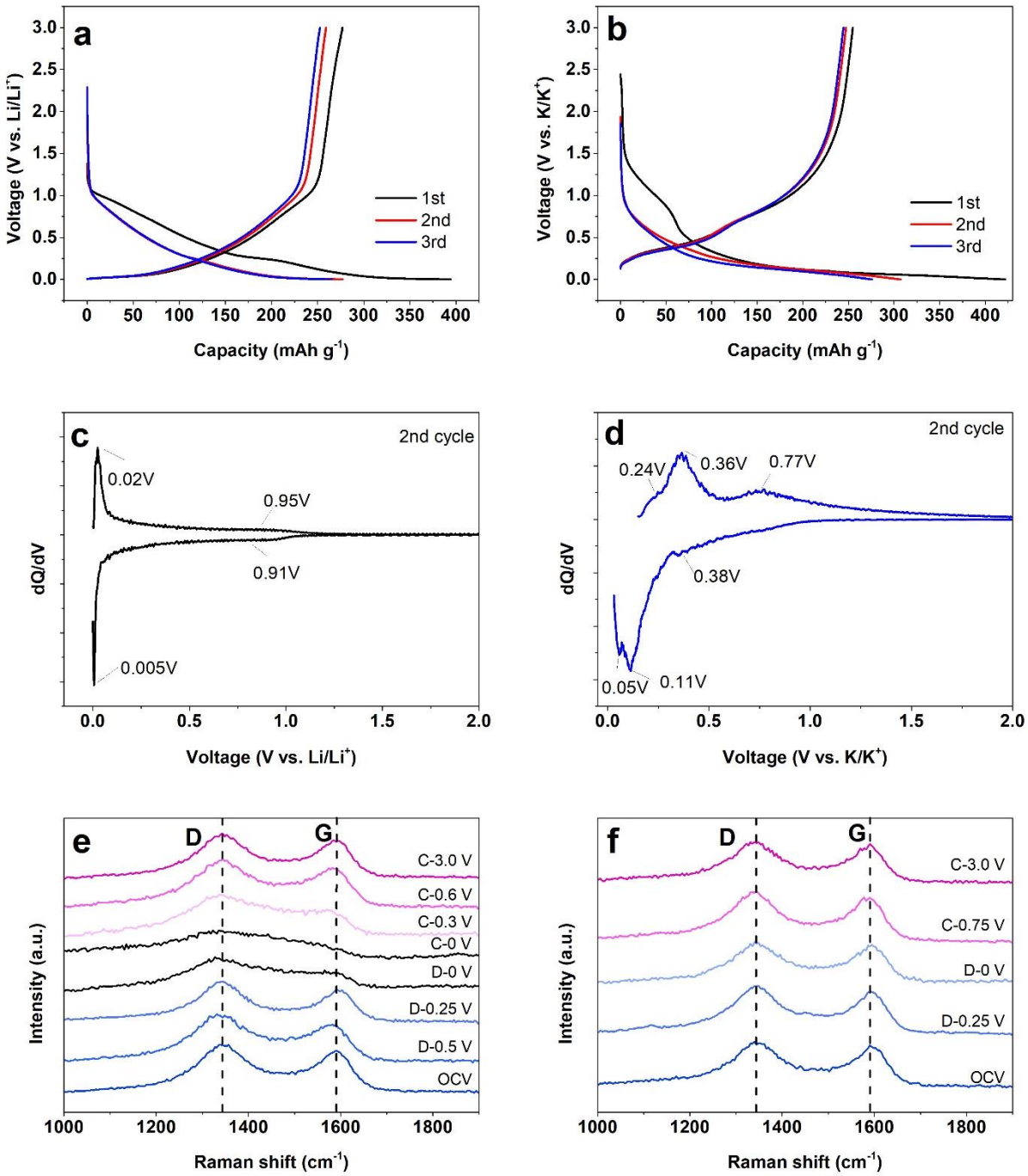

Fig. 6 Galvanostatic charge/discharge curves and dQ/dV plots of LK-200-1350 in (a)(c) Li-ion batteries and (b)(d) K-ion batteries. Selective in-situ Raman spectra of LK-200-1350 in (e) Li-ion batteries and (f) K-ion batteries.

4. Conclusions

Lignin is explored as a precursor for hard carbon preparation, and the corresponding Na-ion storage behavior is investigated. Effect of pre-treatment under air on the microstructure of hard carbon is systematically studied. The optimized pre-oxidation temperature, i.e., 200 °C, resulted in the significantly improved performance, which delivers a capacity of 307 mAh g^{-1} in PC and 336.4 mAh g^{-1} in glyme when charge/discharge at 25 mA g^{-1}. The rate capability is also greatly enhanced, a capacity of 235.6 mAh g^{-1} at 2000 mA g^{-1} is obtained thanks to the dilated layer distance. Moreover, stable cyclic performance is obtained, showing minor fading for 250 cycles. The Na ion storage mechanism is probed by in-situ Raman, which suggests the co-occurrence of Na ion adsorption and pore filling. The comparison with behaviors in Li and K ion batteries indicates the similarities of alkali-metal ion storage at high voltages, which is dominated by the ion adsorption/desorption. A disparity is found at the low voltage, necessitating the delicate microstructure design of hard carbon anode for various types of batteries.

Acknowledgements

This work is supported by the Innovation and Technology Commission (ITF Project ITS/029/17), the Hong Kong Research Grants Council through the Early Career Scheme (Project No. 25215918), the Key Project for Basic Research of Shenzhen (No. JCYJ20170818104125570), and the Hong Kong Polytechnic University (Grant 1-ZE83).

References

[1] X. Wu, D.P. Leonard, X. Ji, Emerging Non-Aqueous Potassium-Ion Batteries: Challenges and Opportunities, Chem. Mater. 29 (2017) 5031–5042.

[2] D. Kundu, E. Talaie, V. Duffort, L.F. Nazar, The Emerging Chemistry of Sodium Ion Batteries for Electrochemical Energy Storage, Angew. Chemie Int. Ed. 54 (2015) 3431–3448.

[3] D. Larcher, J. Tarascon, Towards greener and more sustainable batteries for electrical energy storage, Nat. Chem. 7 (2014) 19–29.

[4] C.P. Grey, J.M. Tarascon, Sustainability and in situ monitoring in battery development, Nat. Mater. 16 (2017) 45–56.

[5] Y. You, X.L. Wu, Y.X. Yin, Y.G. Guo, High-quality Prussian blue crystals as superior cathode materials for room-temperature sodium-ion batteries, Energy Environ. Sci. 7 (2014) 1643–1647.

[6] L. Wang, J. Song, R. Qiao, L.A. Wray, M.A. Hossain, Y. De Chuang, et al. Rhombohedral Prussian white as cathode for rechargeable sodium-ion batteries, J. Am. Chem. Soc. 137 (2015) 2548–2554.

[7] J. Qian, C. Wu, Y. Cao, Z. Ma, Y. Huang, X. Ai, et al. Prussian Blue Cathode Materials for Sodium-Ion Batteries and Other Ion Batteries, Adv. Energy Mater. 8 (2018) 1702619.

[8] G. Yan, S. Mariyappan, G. Rousse, Q. Jacquet, M. Deschamps, R. David, et al. Higher energy and safer sodium ion batteries via an electrochemically made disordered $Na_3V_2(PO_4)_2F_3$ material, Nat. Commun. 10 (2019) 585.

[9] C. Zhu, C. Wu, C.C. Chen, P. Kopold, P.A. Van Aken, J. Maier, et al. A High Power-High Energy $Na_3V_2(PO_4)_2F_3$ Sodium Cathode: Investigation of Transport Parameters, Rational Design and Realization, Chem. Mater. 29 (2017) 5207–5215.

[10] M. Sathiya, J. Thomas, D. Batuk, V. Pimenta, R. Gopalan, J. Tarascon, Dual Stabilization and Sacrificial Effect of Na_2CO_3 for Increasing Capacities of Na-Ion Cells Based on P2-Na_xMO_2 Electrodes, Chem. Mater. 29 (2017) 5948–5956.

[11] U. Maitra, R.A. House, J.W. Somerville, N. Tapia-Ruiz, J.G. Lozano, N. Guerrini, et al. Oxygen redox chemistry without excess alkali-metal ions in $Na_{2/3}[Mg_{0.28}Mn_{0.72}]O_2$, Nat. Chem. 10 (2018) 288–295.

[12] M. Bianchini, E. Gonzalo, N.E. Drewett, N. Ortiz-Vitoriano, J.M. López del Amo, F.J. Bonilla, et al. Layered P2–O3 sodium-ion cathodes derived from earth abundant elements, J. Mater. Chem. A. 6 (2018) 3552–3559.

[13] E. Irisarri, A. Ponrouch, M.R. Palacin, Review—Hard Carbon Negative Electrode Materials for Sodium-Ion Batteries, J. Electrochem. Soc. 162 (2015) A2476–A2482.

[14] D.A. Stevens, J.R. Dahn, High Capacity Anode Materials for Rechargeable Sodium-Ion Batteries, J. Electrochem. Soc. 147 (2000) 1271-1273.

[15] Q. Wang, X. Zhu, Y. Liu, Y. Fang, X. Zhou, J. Bao, Rice husk-derived hard carbons as high-performance anode materials for sodium-ion batteries, Carbon 127 (2018) 658–666.

[16] A. Raj K, M.R. Panda, D.P. Dutta, S. Mitra, Bio-derived mesoporous disordered carbon: An excellent anode in sodium-ion battery and full-cell lab prototype, Carbon 143 (2019) 402–412.

[17] X. Lin, X. Du, P.S. Tsui, J.Q. Huang, H. Tan, B. Zhang, Exploring room- and low-temperature performance of hard carbon material in half and full Na-ion batteries, Electrochim. Acta. 316 (2019) 60–68.

[18] I. Izanzar, M. Dahbi, M. Kiso, S. Doubaji, S. Komaba, I. Saadoune, Hard carbons issued from date palm as efficient anode materials for sodium-ion batteries, Carbon 137 (2018) 165–173.

[19] X. Dou, I. Hasa, M. Hekmatfar, T. Diemant, R.J. Behm, D. Buchholz, et al. Pectin, Hemicellulose, or Lignin? Impact of the Biowaste Source on the Performance of Hard Carbons for Sodium-Ion Batteries, ChemSusChem. 10 (2017) 2668–2676.

[20] C. Marino, J. Cabanero, M. Povia, C. Villevieille, Biowaste Lignin-Based Carbonaceous Materials as Anodes for Na-Ion Batteries, J. Electrochem. Soc. 165 (2018) A1400–A1408.

[21] Y. Li, Y.S. Hu, H. Li, L. Chen, X. Huang, A superior low-cost amorphous carbon anode made from pitch and lignin for sodium-ion batteries, J. Mater. Chem. A. 4 (2016) 96–104.

[22] Y. Wang, N. Xiao, Z. Wang, Y. Tang, H. Li, M. Yu, et al.Ultrastable and high-capacity carbon nanofiber anodes derived from pitch/polyacrylonitrile for flexible sodium-ion batteries, Carbon 135 (2018) 187–194.

[23] C. Matei Ghimbeu, B. Zhang, A. Martinez de Yuso, B. Réty, J.M. Tarascon, Valorizing low cost and renewable lignin as hard carbon for Na-ion batteries: Impact of lignin grade, Carbon 153 (2019) 634–647.

[24] Y. Lu, C. Zhao, X. Qi, Y. Qi, H. Li, X. Huang, et al. Pre-Oxidation-Tuned Microstructures of Carbon Anodes Derived from Pitch for Enhancing Na Storage Performance, Adv. Energy Mater. 8 (2018) 1800108.

[25] H. Yamamoto, S. Muratsubaki, K. Kubota, M. Fukunishi, H. Watanabe, J. Kim, et al.

Synthesizing higher-capacity hard-carbons from cellulose for Na- and K-ion batteries, J. Mater. Chem. A. 6 (2018) 16844–16848.

[26] M. Carboni, J. Manzi, A.R. Armstrong, J. Billaud, S. Brutti, R. Younesi, Analysis of the Solid Electrolyte Interphase on Hard Carbon Electrodes in Sodium- Ion Batteries, ChemElectroChem. 6 (2019) 1745–1753.

[27] E. Memarzadeh Lotfabad, P. Kalisvaart, A. Kohandehghan, D. Karpuzov, D. Mitlin, Origin of non-SEI related coulombic efficiency loss in carbons tested against Na and Li, J. Mater. Chem. A. 2 (2014) 19685–19695.

[28] J. Huang, X. Guo, X. Du, X. Lin, J.Q. Huang, H. Tan, et al. Nanostructures of solid electrolyte interphases and their consequences for microsized Sn anodes in sodium ion batteries, Energy Environ. Sci. 12 (2019) 1550–1557.

[29] B. Zhang, C.M. Ghimbeu, C. Laberty, C. Vix-Guterl, J.-M. Tarascon, Correlation Between Microstructure and Na Storage Behavior in Hard Carbon, Adv. Energy Mater. 6 (2016) 1501588.

[30] Y. Li, Y.-S. Hu, M.-M. Titirici, L. Chen, X. Huang, Hard Carbon Microtubes Made from Renewable Cotton as High-Performance Anode Material for Sodium-Ion Batteries, Adv. Energy Mater. 6 (2016) 1600659.

[31] S. Qiu, L. Xiao, M.L. Sushko, K.S. Han, Y. Shao, M. Yan, X. Liang, L. Mai, J. Feng, Y. Cao, X. Ai, H. Yang, J. Liu, Manipulating Adsorption-Insertion Mechanisms in Nanostructured Carbon Materials for High-Efficiency Sodium Ion Storage, Adv. Energy Mater. 7 (2017) 1700403.

[32] H. Lu, F. Ai, Y. Jia, C. Tang, X. Zhang, Y. Huang, H. Yang, Y. Cao, Exploring Sodium-Ion Storage Mechanism in Hard Carbons with Different Microstructure Prepared by Ball-Milling Method, Small. 14 (2018) 1802694.

[33] C. Bommier, T.W. Surta, M. Dolgos, X. Ji, New Mechanistic Insights on Na-Ion Storage in Nongraphitizable Carbon, Nano Lett. 15 (2015) 5888–5892.

[34] J.C. Chacón-Torres, L. Wirtz, T. Pichler, Manifestation of charged and strained graphene

layers in the Raman response of graphite intercalation compounds, ACS Nano. 7 (2013) 9249–9259.

[35] M. Inaba, H. Yoshida, Z. Ogumi, T. Abe, Y. Mizutani, M. Asano, In Situ Raman Study on Electrochemical Li Intercalation into Graphite, J. Electrochem. Soc. 142 (1995) 20-26.

[36] C. Sole, N.E. Drewett, L.J. Hardwick, *In situ* Raman study of lithium-ion intercalation into microcrystalline graphite, Faraday Discuss. 172 (2014) 223–237.

[37] P. Bai, Y. He, X. Zou, X. Zhao, P. Xiong, Y. Xu, Elucidation of the Sodium-Storage Mechanism in Hard Carbons, Adv. Energy Mater. 8 (2018) 1703217.

[38] B. Zhang, Y. Yu, Z.L. Xu, S. Abouali, M. Akbari, Y.B. He, et al. Correlation between atomic structure and electrochemical performance of anodes made from electrospun carbon nanofiber films, Adv. Energy Mater. 4 (2014) 1301448.

[39] X. Lin, J. Huang, B. Zhang, Correlation between the microstructure of carbon materials and their potassium ion storage performance, Carbon 143 (2019) 138–146.